Attitude Control Calibration and Experiment Testbed to Characterize Attitude Determination and Control System Performance

Jordan. H. Hsieh, Jing-Yuan Huang, Thomas Yen, Sam Lee, Austin Chang, Luke Hou
Tensor Tech CO., LTD.
3F.-1, No. 211, Sec. 2, Anhe Rd., Da'an Dist., Taipei City 106056, Taiwan (R.O.C.); +886 229319383
jordan@tensortech.com.tw

ABSTRACT

This paper describes the design, development, and construction of an attitude control testbed to investigate the performance of ADCS. The Testbed consists of three instruments, an air-bearing platform, a Helmholtz cage, and an AM0 spectrum solar simulator. The Testbed in this research features the capability to measure the mass properties of the tested satellite. One of the motivations of this paper is to share the experience while building this highly automated Testbed. Finally, the procedure of the mass properties measurement will be well described in this paper.

I. INTRODUCTION

Attitude Determination and Control System (ADCS) is a crucial subsystem of satellites for orientation control and pointing stability. For example, earth observation satellites are required to pinpoint their instruments to specific locations on earth accurately. Also, communication satellites that employ narrow-beam antennas require stringent pointing accuracies to guarantee adequate antenna gain. The ADCS comprises attitude determination sensors such as sun sensor, star tracker, gyroscope, and magnetometer to harvest environmental data and attitude actuators such as reaction wheel (RW), magnetorquer, and control moment gyroscope (CMG) to adapt the orientation based on angular momentum conservation law.

In the operational phase, the ADCS computer on board will calculate the current attitude of the satellite based on the environmental data measured by the sensors. After the pointing vector is determined, the ADCS computer will commend the attitude actuator for increasing or decreasing the angular momentum storage according to the current pointing mode. Over time, the so-called indirect actuators, e.g., RWs and CMGs, requires to be desaturated by the direct actuators, e.g., magnetorquers and thrusters, when the disturbance torque is accumulated by the gravity gradient, solar-radiation pressure, geomagnetic field, and atmospheric drag.

Despite the importance of the ADCS, it is one of the easy failing systems during mission operation. Aiming to minimize the technical risk of a system failure, system engineers begin to reproduce the orbital environment condition to test and calibrate their ADCS in the laboratory. Consequently, three orbital conditions have been reproduced: sunlight on the orbit, geomagnetic field, and nearly frictionless rotational degrees of freedom

through a testbed, which comprises the solar simulator, Helmholtz cage, and air bearing platform, respectively.

This paper introduces an air-bearing-based Attitude Control Experiment and Calibration Testbed from Tensor Tech CO., LTD. The common factors for ADCS failure are described in chapter II. In chapter III, the working principle of the air-bearing and the sensors onboard the air-bearing table are introduced. The Helmholtz cage, solar simulator, and mass properties measurement are discussed in chapters IV, V, and VI, respectively.

II. FACTORS FOR ADCS FAILURE

Failures of a satellite ADCS are commonly induced by unexpected steady-state errors, longer response time, or even divergence of controlling outcomes. Figure 1 shows the common factors for ADCS failure. Besides the improper calibration of attitude sensors and actuators and the misalignment of system reference frames, inaccurate mass properties are often unaware by system engineers, which may degrade the performance of the ADCS or even lead to the failure of the entire mission.
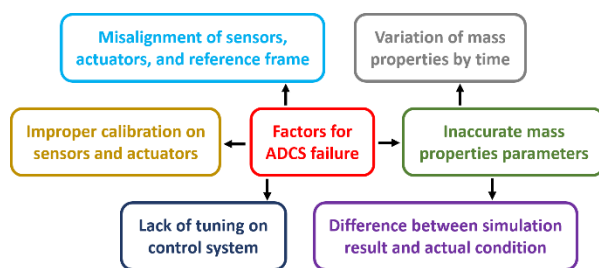

Figure 1: Common factors for ADCS failure.

The mass properties, including the total mass, the center of mass (COM), the moment of inertia (MOI), and the

product of inertia (POI), are critical factors when describing the mechanical characteristics of a satellite. The parameters mentioned above have to be specified during propagating the attitude control algorithms whether the commercial off-the-shelf products are employed, or the components are integrated in-house.

The mass properties are usually obtained through computer-aided design (CAD) simulations. However, two errors will arise in this case compared to the actual situation: time-varying mass properties and simulation accuracy. For the first issue, common causing factors such as thermal variation may cause the deformation of each subsystem due to the inconsistent thermal expand coefficients of each material. Furthermore, propellant consumption will also change the mass properties through an electric or chemical propulsion system. For the second issue, material densities, machining tolerances, satellite assembly errors, and other unpredictable factors cause the inconsistency of mass properties between simulation and actual condition.

Therefore, measuring the mass properties of the assembled satellite is essential to get rid of the issue mentioned above. Propellent consumption caused properties shifting can be calculated and estimated using control techniques embedded in control logic. To tackle these problems, in Figure 2, an attitude control testbed is constructed to measure the COM and MOI of nano-satellites, which will be described and presented in the following chapters.
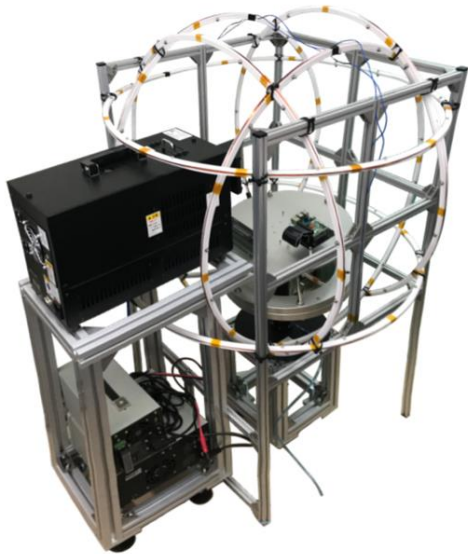

Figure 2: Attitude Control Experiment and Calibration Testbed.

III. AIR-BEARING PLATFORM

Air-bearing platform provides a nearly frictionless environment for testing the attitude actuators while the processor and gyroscope onboard measure the real-time attitude of the platform to validate the performance of the ADCS.

Spherical Air-Bearing System

The spherical air-bearing system comprises an air-bearing hemisphere, base, external compressor, and air preparation filter. Figure 3 shows the air-bearing hemisphere and base utilized in this research.

Figure 3: The air-bearing hemisphere and base by PI (Physik Instrumente) L.P.

An external compressor is responsible for providing pressurized air to the air-bearing base through a pipeline during operation. After the pressurized air reaches the air-bearing base, a thin air layer is formulated between the concave bearing base and convex air-bearing hemisphere, which floats the hemisphere and provide frictionless motion in three rotational degrees of freedom. In Figure 4, the tabletop-type spherical air-bearing system used in this research has unrestrained rotation about the vertical Z-axis and ±45° tilt motion about the horizontal X and Y axes.
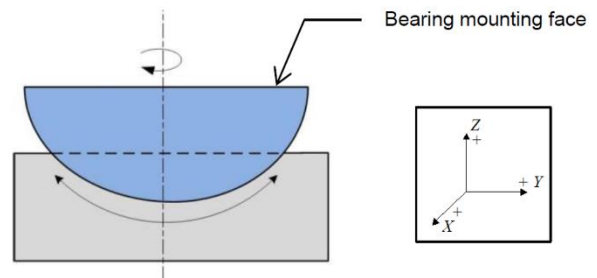

Figure 4: Degrees of freedom and the coordinate system of the spherical air-bearing [1]

In Figure 5, to prevent the system been damaged by the impurity air, an air preparation filter is employed to remove the moisture and airborne particle from the gas inlet before the pressurized airflow is fed into the bearing base. Meanwhile, every low friction air-bearings will exhibit the turbine torque effect, where the air layer between the bearing base and hemisphere has a preferential flow direction that will drive the hemisphere to accelerate in one rotating axis. Therefore, the pressure of the compressor is regulated at an optimum threshold due to the nature of air-bearings.
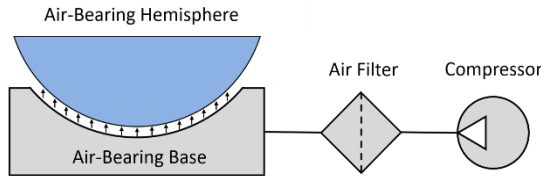

Figure 5: The pneumatic system of the Testbed.

The table and satellite fixer

Figure 6 shows the overlook of the table with a satellite fixer mounted on top of the hemisphere. In Figure 6, the fixer is responsible for holding the satellite rail. There are six socket set screws within the fixture with a PTFE tip to carefully hold the satellite. Each socket set screw is applied moderate torque to prevent any deformation and scratches on the satellite structure. Below the fixer is the delicate triaxial orthogonal shifting mechanism. The shifting mechanism is employed to adjust the composite COM of the satellite body and the air-bearing table to coincide COM with the center of rotation (COR) of air-bearing after the satellite is mounted on the fixer.
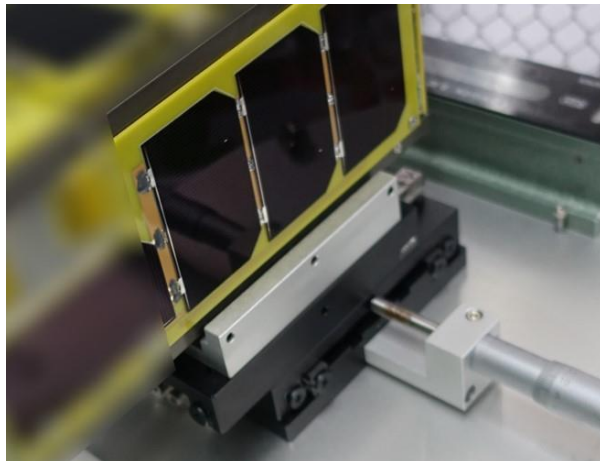

Figure 6: A satellite held by the fixer.

The attitude measurement unit and software are integrated on the air-bearing table. The Testbed architecture is represented in Figure 7, which includes a single-board computer, air-bearing platform, power

management system, solar simulator, and Helmholtz cage with a power source to induce a homogenous magnetic field. The single-board computer supports I²C, Ethernet, and SPI with a transceiver to transmit data and receive commands from the personal computer wirelessly. In this way, the disturbance caused by the wires and connectors can be minimized during operation to prevent any degradation in experiment accuracy and reliability.
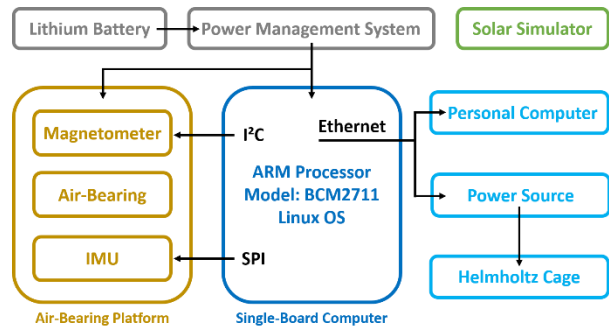

Figure 7: System architecture of the Testbed.

The three-axis magnetometer and IMU, including a triaxial gyroscope and accelerometer, serve as the attitude determination sensor to identify the current attitude of the air-bearing table, while the former is connected to the single-board computer through I²C, and the latter is connected through SPI. The gyroscope used in this paper feature an in-run bias instability of 0.8 degrees per hour and an angular random walk of 0.09 degrees per square root hour. The gyroscope has a constant intrinsic bias, the slope of the integrated Euler angles. This characteristic is shown in Figure 8. However, these integrated Euler angles are not perfectly linear. This non-linearity can be evaluated with two parameters, bias instability and angular random walk. With these two specifications and a Kalman filter combining the acceleration vector which points to the direction of gravity from the earth, the pointing knowledge can be obtained:

1. ~0.1 degrees (1-sigma) of the pointing knowledge error within a 30-second ADCS testing experiment

2. ~0.9 degrees (1-sigma) of the pointing knowledge error within a 1-hour ADCS testing experiment

3. ~1.1 degrees (1-sigma) of the pointing knowledge error within a 1.5-hour ADCS testing experiment

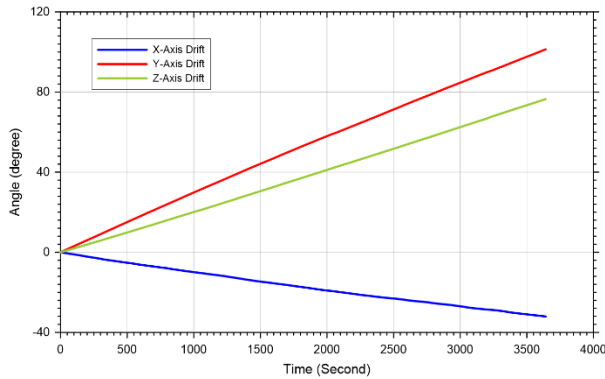It is worth knowing that the variance of the platform attitude determination grows through time.

Figure 8:   The Bias drift of platform velocity.

After mounting the satellite on the air-bearing table through the fixer, the composite COM will drift upward relative to the COR of the air-bearing, likely making the system unstable. To pull down the composite COM approximately to the shared XY-plane (see Figure 4) with the COR and allow the fine adjustment of the triaxial orthogonal shifting mechanism for the COM and COR coincidence, in Figure 9, the ring-shaped mass balancing aluminum plates are attached to the underside of the air-bearing table through four M10 bolts. The number of the attached aluminum plate can be modified to meet satellites of various weights.

Figure 9:   The air-bearing platform.

IV. HELMHOLTZ CAGE

The 3-axis Helmholtz cage is often used in the ADCS testbed to cancel the local geomagnetic field and simulate the magnetic field on the targeted orbit. This equipment is helpful for magnetometer calibration or testing the performance of the magnetorquers.

Magnetic Field Homogeneity

The triaxial Helmholtz cage has six coils surrounding the air-bearing platform in three orthogonal axes. Figure 9 presents the latest design of the Helmholtz cage from Tensor Tech CO., LTD. There is an air-bearing platform located within the Helmholtz cage. To induce a homogeneous magnetic field, the coils are assembled from 32, 36, and 40 turns of the copper enameled wire with a 3 mm diameter for the Z-axis, Y-axis, and X-axis coils, respectively. The copper wires are wrapped in stacked phenol-formaldehyde resin plates made by computer numerical control (CNC) machining. Through CNC machining, the Helmholtz cage can be scaled up quickly to meet various testing requirements without losing the positioning accuracy.
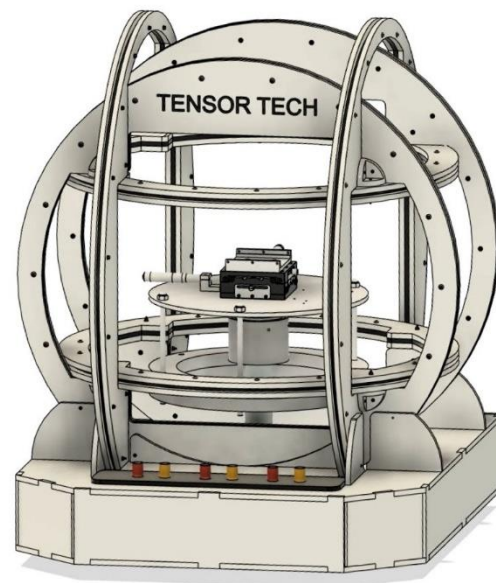

Figure 10: The 3-axis Helmholtz cage from Tensor Tech CO., LTD.

The measurement ensures the magnetic field homogeneity through the magnetic sensor within the cage. In Figures 11 to 13, twenty-seven measuring points (i.e., the three-dimensional matrix in the center of the Helmholtz cage) are selected to test the magnetic field homogeneity of an 800 mm diameter cage. Each measuring point is 100 mm apart. The deviation is defined as the percent variance compared with the middle measuring point from the rest of the twenty-six points. The data in Figures 11 to 13 are acquired when the current of 3 A is passing through each coil. The results show that the deviations are less than 5% compared to the middle measuring point within the 100 cubic millimeters. Some factors produce deviations, for instance, the misalignment of the coils and different lengths of the copper wire. However, the deviation can be controlled and modified
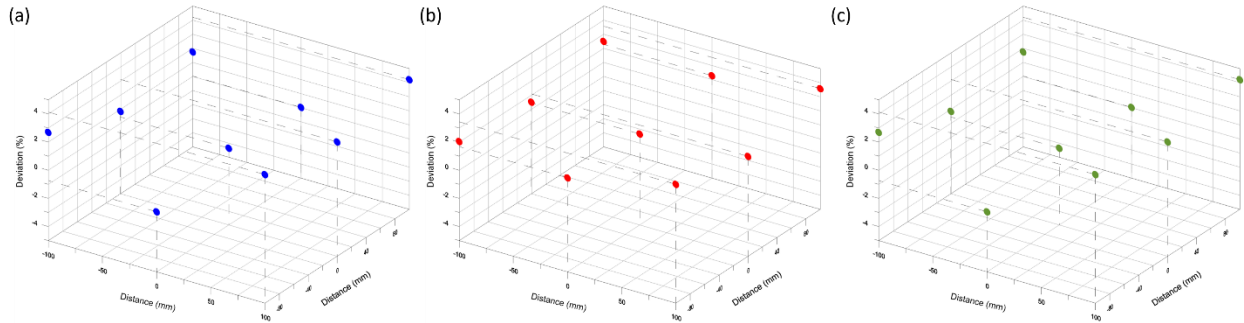
Figure 11: The percent variance of magnetic flux density on the XY-plane at Z = 100 mm compared to the middle measuring point in Figure 12. (a) X-axis coil activated (b) Y-axis coil activated (c) Z-axis coil activated
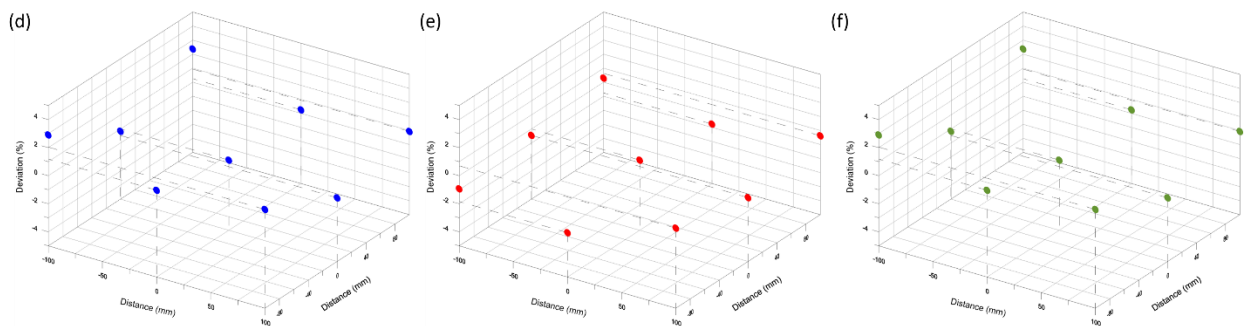

Figure 12: The percent variance of magnetic flux density on the XY-plane at Z = 0 mm compared to the middle measuring point. (d) X-axis coil activated (e) Y-axis coil activated (f) Z-axis coil activated
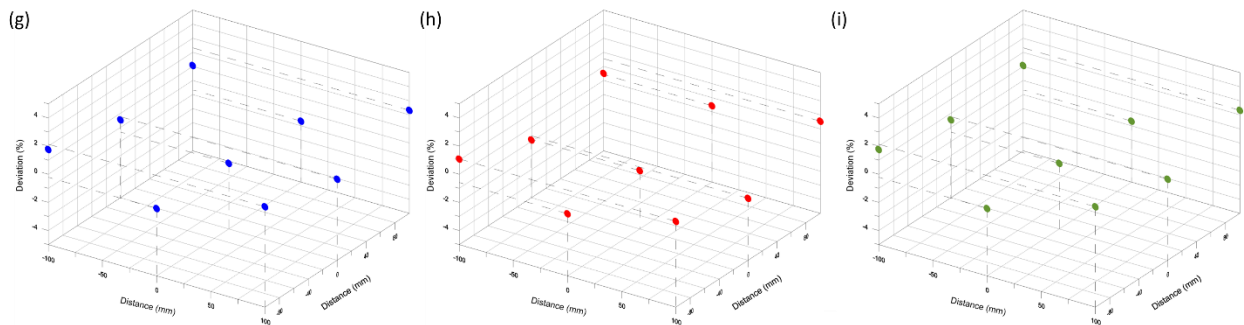

Figure 13: The percent variance of magnetic flux density on the XY-plane at Z = -100 mm compared to the middle measuring point in Figure 12. (g) X-axis coil activated (h) Y-axis coil activated (i) Z-axis coil activated

by scaling up or down the dimension of the Helmholtz cage, producing a homogeneous magnetic field.

Magnetic field linearity and coupling

The linearity of magnetic flux density of different input currents and the deviation of magnetic flux density caused by triaxial coils coupling are present in Figure 14. There are two testing scenarios to investigate the linearity and deviation. For linearity, a set of coils is activated on one axis. Next, sweep the input current to measure the magnetic flux density generated at each current level to confirm the linearity. For deviation, while sweeping the input current on one axis, the coils on the other two axes are activated at the same current level to examine the coupling effect in simultaneous operation, providing a homogeneous triaxial magnetic field. The data shown in Figure 14 are measured on the center point between the coils by magnetic-inductance sensors for X, Y, and Z-axis coils.
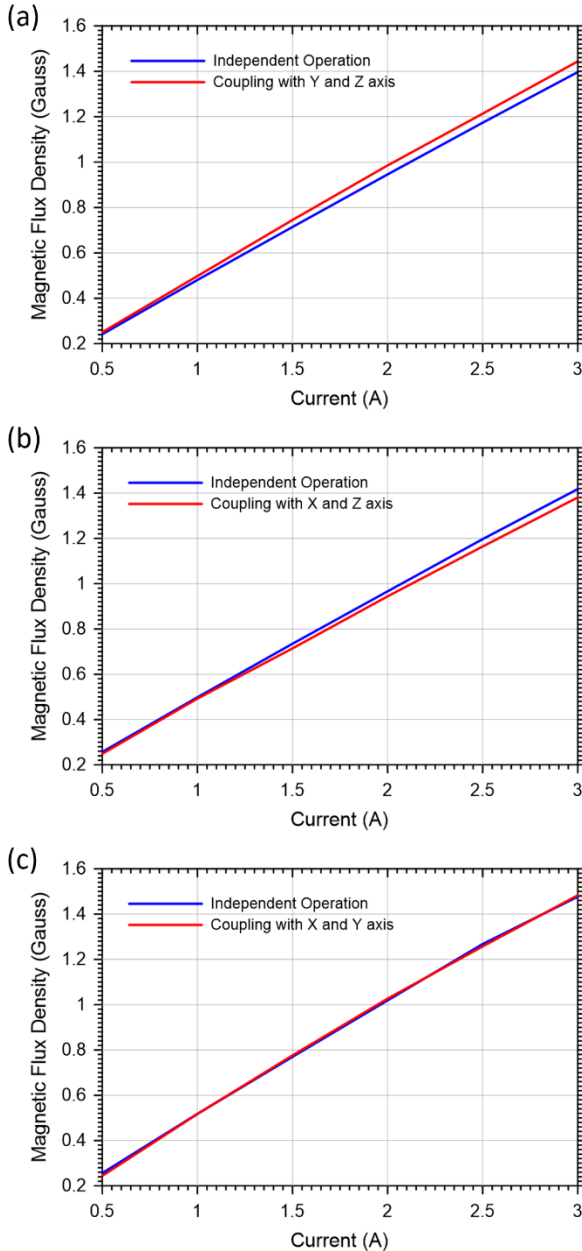
(a)

(b)

(c)

Figure 14: The linearity and deviation of magnetic flux density between independent operation and coupling with the other two axes along with (a) X-axis, (b) Y-axis, and (c) Z-axis.

The testing result shows great linearity in the nominal current input ranging from 0.5 to 3 A. The magnetic flux density along the X-axis is slightly increased by the Y and Z-axis coupling, while the X and Z-axis coupling slightly decreases the Y-axis flux density. Furthermore, there is no noticeable deviation caused by coupling on the Z-axis.

V. SOLAR SIMULATOR

The sunlight spectrum above the atmosphere is different from the spectrum on the ground surface. An AM0 solar simulator is employed in this research to simulate the sunlight from orbit. Figure 15 shows the outlook of the solar simulator to provide a 40 square millimeter light spot. The spatial non-uniformity of total irradiance of the solar simulator utilized in this research is less than 2%, and the time instability and collimation are less than 1% and 4 degrees, respectively.

Figure 15: The solar simulator by SAN-EI Electric Co., Ltd. [2]

When conducting the attitude control experiment, the drift of the light spot center needs to be carefully considered because the sun sensor determines the sun angle based on calculating the center of the light spot. Therefore, in this research, a quad segmented photodiode to capture the drift of the solar simulator. Figure 16 shows that the drift of the light spot center will keep drifting in the first 20 minutes, which reveals that the experiment should be conducted after the solar simulator after turned on for 20 minutes.
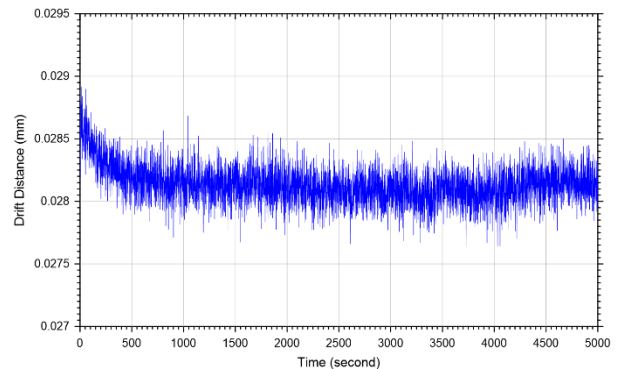

Figure 16: The drift of the light spot center.

The main reason causing this drift is the thermal expansion. After the device is turned on, the thermal deposition on each part and lens will slightly deform by the different thermal expansion coefficients of each

material, including the quad segmented photodiode used to measure the light spot drift.

VI. MASS PROPERTIES MEASUREMENT

One of the Testbed features in this research is integrating a mass properties measurement function. Due to the nature of the low disturbance torque of the air-bearing, the air-bearing platform becomes a suitable candidate for nano-satellite mass properties measurement. The measuring procedure for mass properties of the device under test (DUT) is listed below:

1. Holding the DUT by the fixer on top of the air-bearing table.

2. Importing the total mass of the DUT to the Testbed, which will be measured through the electronic precision scale. The mass properties of the air-bearing will be measured before this step.

3. The algorithm will calculate the composite COM based on the data harvested by the IMU on the platform.

4. The researchers can tune the COM to coincide with the COR through the delicate triaxial orthogonal shifting mechanism on the air-bearing table according to the triaxial value calculated by the algorithm.

5. After the COM coincides with COR, the researchers can attach the precision weights to the air-bearing platform to produce an unbalanced torque. As a consequence, the platform will start to oscillate.

6. The IMU will record the angular velocity and acceleration vector during oscillation for composite COM and MOI calculation.

7. Removing the DUT, repeating step 6 to measure the COM and MOI of the air-bearing platform.

8. Combining the COM and MOI mentioned above in steps 6 and 7, the actual COM and MOI of the DUT can be calculated precisely.

Despite the mass properties of the air-bearing platform having been measured before the procedure, the necessity to re-measure the mass properties of the platform in step 7 after removing the DUT is because the mass properties of the entire platform have been changed while adjusting the delicate triaxial orthogonal shifting mechanism on the air-bearing table.

The data plot in Figure 17 is the angular velocity of a SmallSat ADCS acquired during step 6. By calculating these raw data, the algorithm can derive the mass properties of the DUT.
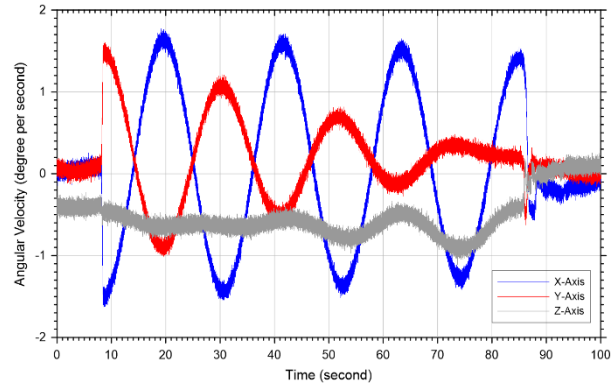

Figure 17: The angular velocity of the platform.

The nominal data update rate of the platform is 2kHz. However, the transceiver is not fast enough to wirelessly transmit the data to the personal computer. Therefore, the researchers have to download these data after the experiment from the single-board computer on the platform.

VII. CONCLUSION

To prevent any system failure and calibrate the ADCS in the laboratory, an air-bearing-based Attitude Control Experiment and Calibration Testbed is developed and constructed by Tensor Tech CO., LTD., which consists of an air-bearing platform to provide a nearly frictionless three rotational degrees of freedom, a triaxial Helmholtz cage that generates a homogeneous magnetic field to cancel the local geomagnetic field and further simulate the magnetic field on the target orbit, and an AM0 spectrum solar simulator is employed to provide sunlight similar to the one above the atmosphere.

One of the Testbed features in this research is that it is capable of measuring the mass properties of the device under test. Because of the low disturbance torque characteristic of air-bearing, the spherical air-bearing platform becomes an ideal selection to measure the mass properties of nano-satellite.

Another feature of the Testbed in this research is that it is highly automated, integrating the air-bearing platform, Helmholtz cage, solar simulator, single-board computer, IMU, power management system, and personal computer with a mass properties calculation algorithm that has the scalability for the more extensive Testbed. As a result, this Testbed can speed up the research and development process of a satellite and significantly reduce the resources required to invest in a single mission.

References

1. PI L.P. (2019). Plglide HB Hemispherical Air Bearings: User manual. Retrieved from https://www.physikinstrumente.com/en/.

2. SAN-EI Electric Co., Ltd. (2017) XES-40S3 AAA Class Portable Solar Simulator: User manual. Retrieved from https://www.san-eielectric.co.jp/